



Simplify your imaging workflows

**Make research imaging workflows accessible, traceable,
and secure with Athena Software for Core Imaging Facilities.**

Thermo Scientific™ Athena Software is a premium imaging data management platform designed for core imaging facilities that support materials science research.

Athena Software ensures traceability of images, metadata, and experimental workflows through an intuitive and collaborative web interface.

Find out more at thermofisher.com/athena

ThermoFisher
SCIENTIFIC

High-Efficiency Dielectric Huygens' Surfaces

Manuel Decker, Isabelle Staude,* Matthias Falkner, Jason Dominguez, Dragomir N. Neshev, Igal Brener, Thomas Pertsch, and Yuri S. Kivshar

Optical metasurfaces have developed as a breakthrough concept for advanced wave-front engineering enabled by subwavelength resonant nanostructures. However, reflection and/or absorption losses as well as low polarization-conversion efficiencies pose a fundamental obstacle for achieving high transmission efficiencies that are required for practical applications. Here, for the first time to our knowledge, highly efficient all-dielectric metasurfaces are demonstrated for NIR frequencies using arrays of silicon nanodisks as metaatoms. The main features of Huygens' sources are employed, namely, spectrally overlapping crossed electric and magnetic dipole resonances of equal strength, to demonstrate Huygens' surfaces with full transmission-phase coverage of 360° and near-unity transmission. Full-phase coverage combined with high efficiency in transmission are experimentally confirmed. Based on these key properties, all-dielectric Huygens' metasurfaces can become a new paradigm for flat optical devices, including beam-steering, beam-shaping, and focusing, as well as holography and dispersion control.

1. Introduction

More than 300 years ago Huygens proposed that every point on a wave front acts a secondary source of outgoing waves.^[1] Notably, despite its simplicity, Huygens' principle already allows for the derivation of the fundamental laws of diffraction and reflection and intuitively explains how components such as conventional lenses, which are based on the accumulation of (position dependent) phase delay during wave propagation, can be used to shape an emerging wave front in a desired way. A more rigorous formulation of the Huygens' principle developed by Love more than 200 years later^[2] reveals that in order to achieve purely forward-propagating elementary waves, as required by

the Huygens' principle, each individual elementary source should be described as an electrically small antenna that radiates the far-fields of crossed electric and magnetic dipoles (Huygens' sources).^[2–4] While these elementary sources were originally introduced as fictitious entities, an actual physical implementation of Huygens' sources can be achieved using polarizable subwavelength particles that sustain both electric and magnetic dipolar resonances.^[3–6] Arranging many of such particles in a plane furthermore allows for creating effective Huygens' surfaces – reflectionless sheets that can be used to manipulate electromagnetic waves by controlling the resonant properties of the particles as a function of position.^[5,6]

Only recently, experimental demonstrations of metallic Huygens' surfaces at microwave frequencies,^[5] where the dis-

sipative losses of metals are negligible, have been presented, and design concepts that allow bringing plasmonic Huygens' surfaces to the mid-IR spectral range have also been developed.^[6] However, transferring this powerful concept to near-IR and visible wavelengths remains challenging.^[7] This challenge originates from the weak magnetic response of natural materials at optical frequencies. Even for plasmonic nanoparticles, despite their capability to provide a magnetic permeability that significantly deviates from unity,^[8,9] the critical combination of spectrally overlapping pure magnetic and electric dipole resonances of equal strength, as it is required for resonant Huygens' sources, has not been realized yet. Furthermore, down-scaling the suggested structures^[5,6] to near-IR or even visible operation wavelengths is further hindered by the significant increase of dissipative losses of plasmonic structures at optical frequencies limiting their performance.^[7] Overcoming these limitations is essential for realizing efficient Huygens' metasurfaces at near-IR operation wavelengths. A promising path to solve this problem is the use of dielectric nanoparticles, or dielectric resonator antennas, that have been studied in the microwave and radio-frequency range^[10] and have recently been brought to optical frequencies.^[11–16] Importantly, dielectric nanoparticles can support both electric and magnetic dipolar Mie-type modes^[11–21] while, at the same time, exhibiting very low intrinsic losses.

We here present and demonstrate a new route for implementing Huygens' sources at optical frequencies utilizing the strong electric and magnetic resonances of high-permittivity all-dielectric nanodisks in the near-IR spectral range (Figure 1).

Dr. M. Decker, Dr. I. Staude, Prof. D. N. Neshev,
Prof. Y. S. Kivshar
Nonlinear Physics Centre
Research School of Physics and Engineering
The Australian National University
Canberra, ACT 0200, Australia
E-mail: isabelle.staude@anu.edu.au

M. Falkner, Prof. T. Pertsch
Institute of Applied Physics
Abbe Center of Photonics
Friedrich-Schiller-Universität Jena
07743, Jena, Germany

J. Dominguez, Dr. I. Brener
Center for Integrated Nanotechnologies
Sandia National Laboratories
Albuquerque, NM 87185, USA

DOI: 10.1002/adom.201400584



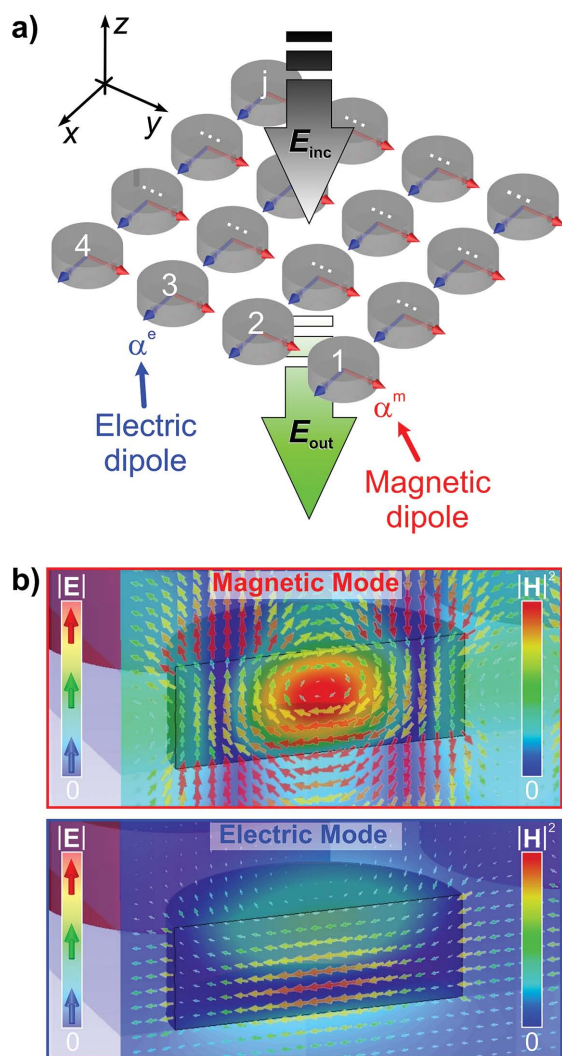


Figure 1. a) Schematic of an (infinite) array of nanodisks represented as electric and magnetic dipoles with the polarizabilities α^e and α^m for x-polarized incident light that describes a Huygens' metasurface. b) Electric (colored arrows) and magnetic (plain color coded) field distributions of the magnetic (top) and electric (bottom) mode of a silicon-nanodisk metasurface. The two modes are dominated by a strong magnetic and electric dipole moment, respectively, located in the center of the nanodisk.

These resonances can be tuned via the nanodisk geometry, which allows for tailoring of directional scattering.^[19] Here we show that by controlling the intrinsic properties of the electric and magnetic dipole resonances, i.e., their relative electric and magnetic polarizabilities and their quality factors in addition to their spectral position, we can design silicon nanodisks to behave as near-ideal Huygens' sources. This allows us to realize effective all-dielectric Huygens' metasurfaces, i.e., subwavelength arrangements of Huygens' sources that lack dissipative losses and also suppress unwanted reflections. At the same time they provide full 2π coverage for the phase shift imposed onto a transmitted light wave without relying on cross-polarization schemes and, thus, without suffering from polarization-conversion losses as most of the plasmonic counterparts.^[22–28] Consequently, silicon-nanodisk Huygens' metasurfaces in

principle allow for light-wave manipulation with ideally 100% transmission efficiency and can also provide almost arbitrary spatial distributions of phase discontinuities depending on the design of the metaatoms at each position. The latter aspect is of particular interest for wave-front manipulation applications. Indeed, it has been shown recently that tailoring the spatial distribution of phase discontinuities with metasurfaces allows for the realization of flat optical devices.^[22–33] However, the big obstacle in rendering these (mostly plasmonic) devices practical for real-world applications is their low efficiency, which stems from reflections, dissipative losses, and/or low polarization-conversion yield. All-dielectric optical Huygens' metasurfaces eliminate these restrictions and, hence, can be used for high-efficiency wave-front manipulation at near-IR frequencies. To demonstrate this concept experimentally we fabricate silicon nanodisks as metaatoms, which we arrange in a 2D subwavelength array. By direct phase-resolved transmittance measurements we experimentally demonstrate the characteristic properties of a Huygens' metasurface, i.e., a complete phase coverage from 0 to 2π for nanodisks with spectrally overlapping resonances accompanied by record resonant transmission efficiencies of more than 55% which is more than a factor of 3 better than in all plasmonic phase-gradient metasurfaces at optical frequencies to date.^[7,22–24,26–28,30] Our experimental results are supported by numerical calculations, indicating that 99% resonant transmission efficiency can be achieved for a Huygens' metasurface consisting of silicon nanodisks embedded into an optimized dielectric environment. Furthermore, we present an analytical model, which does not only provide a rigorous explanation of our findings but furthermore shows that, for electric and magnetic dipole resonances with identical intrinsic properties, ideally 100% resonant transmittance accompanied by full 2π phase coverage can be achieved.

2. Analytical Model of a Resonant Huygens' Metasurface

In order to gain a fundamental understanding of the response of a Huygens' metasurface, we first discuss the full complex response of an idealized subwavelength array of loss-less nanodisk metaatoms with electric and magnetic dipole resonances of equal strength and width under plane-wave illumination. Our analytical model is based on a coupled discrete dipole approach^[34] where each individual nanodisk is represented by an ideal Huygens' source, i.e., a pair of electric and magnetic dipoles oriented in x and y direction with polarizabilities that follow a Lorentzian frequency dependence with resonance positions ω_e and ω_m and damping parameters γ_e and γ_m , respectively. The two dipoles are arranged in an infinite subwavelength 2D-square lattice forming the silicon-nanodisk Huygens' metasurface [Figure 1a]. As such, our analytical approach goes far beyond purely numerical mode-analysis approaches predicting mode properties or mode positions for single nanodisk antennas as presented in ref. [19], for example. Instead, our analytical approach enables a complete description and fundamental understanding of a loss-less Huygens' metasurface. Hence, we calculate an analytical expression for the field-transmittance and reflection coefficients as a function of frequency ω (see the Experimental Section), yielding

$$t = 1 + \frac{2i \cdot \gamma_e \cdot \omega}{\omega_e^2 - \omega^2 - 2i\gamma_e \omega} + \frac{2i \cdot \gamma_m \cdot \omega}{\omega_m^2 - \omega^2 - 2i\gamma_m \omega} \quad (1)$$

and

$$r = \frac{2i \cdot \gamma_e \cdot \omega}{\omega_e^2 - \omega^2 - 2i\gamma_e \omega} - \frac{2i \cdot \gamma_m \cdot \omega}{\omega_m^2 - \omega^2 - 2i\gamma_m \omega} \quad (2)$$

respectively. Importantly, the last terms in Equations (1) and (2) stem from the contribution of the magnetic dipoles whereas the electric contributions are associated with the preceding terms. Evidently, the sign of the electric field component of the magnetic-dipole mode radiated in forward *versus* backward direction is different while the sign of the electric-field component of the electric-dipole resonance is the same for both directions. This aspect is, indeed, a known feature discriminating magnetic and electric dipole radiation and can be utilized to create, e.g., an optical magnetic mirror.^[35,36] The transmitted-power spectrum T (transmittance intensity) is determined by the interference of the collective magnetoelectric response of the metasurface and the incident plane wave.

Figure 2a,b shows the full spectral (amplitude and phase) response (green) obtained by our analytical approach for an ideal loss-less metasurface with spectrally separate electric ($\lambda_{el} = 1400$ nm) and magnetic ($\lambda_{mag} = 1200$ nm) resonances of equal strength and width. Interference with the incident plane wave results in the expected two transmittance-intensity dips

shown as green line in Figure 2a. Correspondingly, the phase response of the transmitted field shows resonant behavior at the corresponding resonance wavelengths with a maximum phase change in resonance of π for both resonances. Figure 2c further visualizes the resonance signature in terms of an electric-field vector diagram for the nonoverlap case at a selected wavelength ($\lambda = 1252$ nm).

Figure 2d–f shows the corresponding diagrams for the case of spectrally overlapping electric and magnetic resonances of equal strength and width. In sharp contrast to the case of separate resonances, we observe a flat line with a transmittance-intensity of unity for this ideal case. More importantly, the phase response of the total electric field changes drastically as evident from Figure 2e and undergoes a phase change of 2π within 200 nm around the resonance wavelength – this is double the phase shift that can be achieved by a single (electric or magnetic) resonance. Notably, although the resonant behavior observed in the phase of the transmitted light is not reflected in its amplitude, our results are consistent with causality as expressed by the Kramers–Kronig relations. In order to visualize how the contributions of the electric and the magnetic resonances in combination with the incident plane wave lead to unity resonant transmittance-intensity we again plotted the vector diagram of the electric field components in Figure 2f for the resonant case at $\lambda = 1300$ nm. Evidently, the electric field component of the incident plane wave is eliminated by destructive interference with one of the two dipole resonances

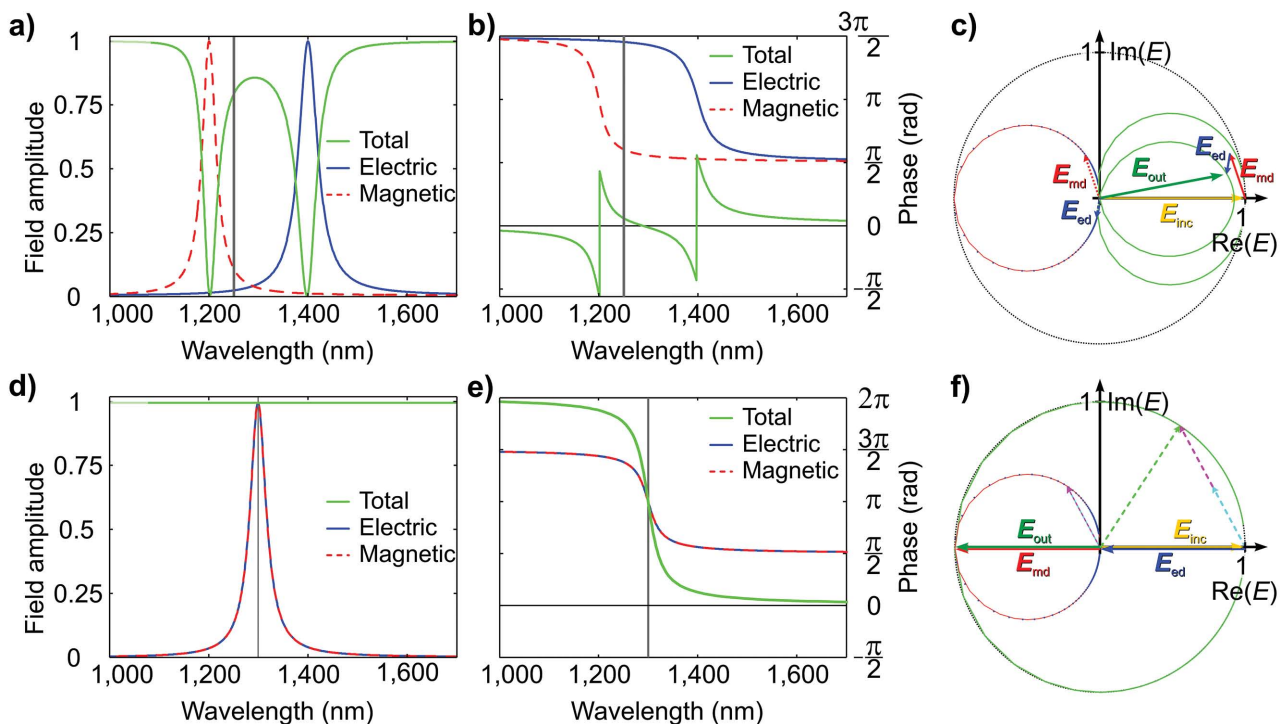


Figure 2. a) Analytical results for the electric-field amplitude of the transmitted light (green) and the contributions of the electric (blue) and magnetic (red) resonances for the case of nonoverlapping resonances. b) Analytical phase spectrum of the transmitted electric field (green) and the electric (blue) and magnetic (red) response. c) Vector diagram depicting the decomposition of the electric-field vector (E_{out} , green) into the contributions from the electric (E_{ed} , blue) and magnetic (E_{md} , red) resonances and the incident wave (E_{inc} , yellow) at $\lambda = 1252$ nm (gray line in a) and b)). The transmitted field is depicted as green line. d)–f) Corresponding diagrams for the case of spectrally overlapping electric and magnetic resonances: d) Field amplitudes, e) phase spectrum, and f) vector diagram at $\lambda_{el} = \lambda_{mag} = 1300$ nm. The electric- and magnetic-field components for a second wavelength are also plotted (cyan and magenta). See the Supporting Information for movies illustrating the evolution of a)–f) with wavelength.

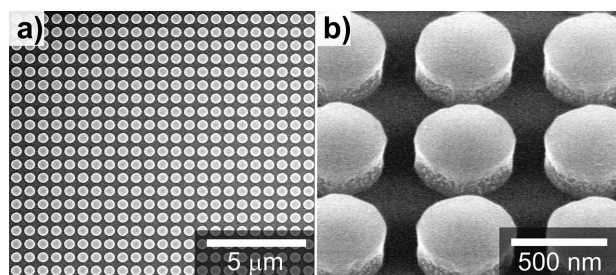


Figure 3. a) Top-view and b) side-view electron micrographs of a typical silicon-nanodisk sample with a disk radius of $r_d \approx 242$ nm, a disk height of $h = 220$ nm, and a lattice constant of $a \approx 666$ nm.

while the second dipole resonance provides unity field amplitude that is out-of-phase with the incident plane wave (red and blue arrows). The sum of the electric field components of the plane wave and of the electric and magnetic resonances lies on an $|\mathbf{E}_{\text{out}}| = 1$ circle independent of wavelength, which is equivalent to the flat $T = 1$ line in transmittance shown in Figure 2d. Importantly, this behavior cannot be observed for any single dipolar resonance but is characteristic for the interference of electric and magnetic dipole resonances of equal strength. As such our results are a direct manifestation of the magnetic-dipole radiation characteristics of the magnetic resonance of the Huygens' source.

3. Experimental Results

In order to experimentally realize low-loss Huygens' metasurfaces for near-IR frequencies we choose silicon nanodisks as metaatoms since they allow for tailoring the spectral positions of their electric and magnetic dipole-type modes with respect to each other via controlling their aspect ratio.^[19] Silicon, in particular, is an attractive material choice owing to its extremely low dissipative losses above 1.1 μm wavelength and its prevalence in modern technology.

We use standard silicon-on-insulator technology (see the Experimental Section) to fabricate subwavelength lattices of silicon nanodisks with different disk radii r_d on a 2- μm -thick

silicon-oxide layer and investigate the two cases of (1) mode overlap ($r_d \approx 242$ nm) and (2) separate electric and magnetic resonances ($r_d \approx 198$ nm). The lattice constant a of the samples is approximately 666 nm. Scanning-electron micrographs of a typical sample with $r_d \approx 242$ nm are shown in Figure 3.

We then obtain the samples' spectrally resolved transmittance phase with an interferometric white-light spectroscopy setup^[37,38] and the normalized experimental transmittance-intensity ($T_n = T/T_0$) using a conventional white-light spectroscopy setup, respectively (see the Experimental Section). Our experimental measurements of the transmittance-phase spectra are summarized in Figure 4a,b for the nonoverlap and the overlap case, respectively.

Figure 4b experimentally confirms the predicted strong phase response covering the full range from 0 to 2π within a wavelength range of ≈ 200 nm in the measured transmittance-phase response. In this case the electric and magnetic resonances of the silicon-nanodisk metasurface are close to the spectral overlap condition for a nanodisk radius of 242 nm. This is, indeed, the unambiguous fingerprint of a Huygens' metasurface. For the nonoverlap cases ($r_d = 198$ nm) we find two typical single-resonance signatures in the transmittance phase [Figure 4a], each featuring a maximum phase change of π .

To further underpin our analytical and experimental findings we additionally compare our measurements with numerical finite-element calculations (see the Experimental Section). In our numerical calculations we explicitly take into account the influence of the handle wafer. These results are also displayed in Figure 4 as black-dashed lines and show excellent agreement with the experimental spectra for both cases. Particularly, the numerical calculations again confirm the 2π phase coverage for spectrally overlapping modes that has been found in the experiment and the analytical model. In order to clearly identify the transmission efficiencies of the Huygens' metasurface investigated in Figure 4b, i.e., without Fabry–Perot oscillation caused by the handle wafer in the spectrum, we embed the sample in a spin-on glass with a refractive index of $n = 1.4$, and we remove the handle-wafer via a deep reactive-ion etching process.^[39] Figure 5a shows the experimental (red-solid line) and corresponding numerical (black-dashed line) transmittance intensity for this case. Our Huygens' metasurface exhibits

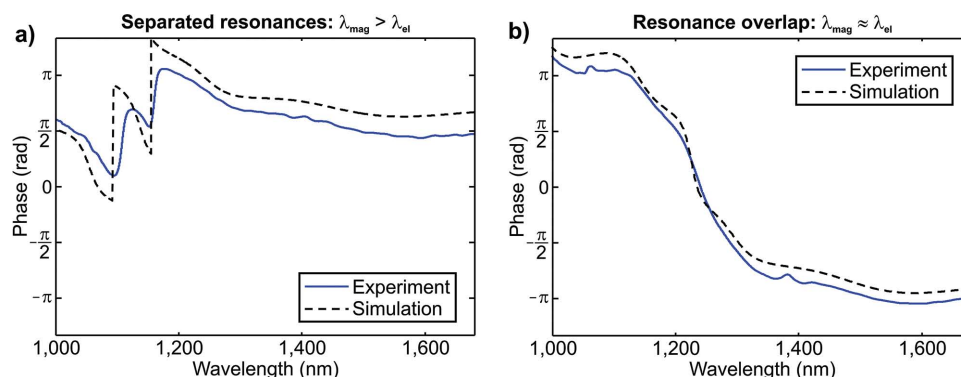


Figure 4. Measured transmittance-phase spectra (blue lines) of the nanodisk metasurfaces with a) 198 nm and b) 242 nm nanodisk radii. The lattice constants ($a \approx 666$ nm) of the two samples are chosen such that the electric and magnetic dipole resonances appear at longer wavelengths than the first Wood anomaly. The black-dashed lines in a) and b) show the corresponding numerical calculations that are in excellent agreement with the experimental results.

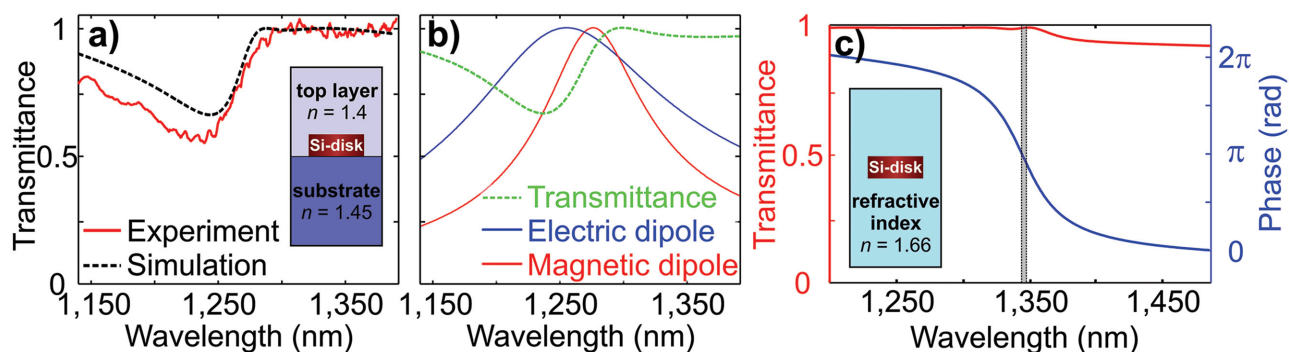


Figure 5. a) Experimental transmittance spectrum of the Huygens' metasurface [overlap case shown in Figure 4b)] embedded in spin-on glass ($n = 1.4$) after handle-wafer removal (red-solid line) and corresponding numerical calculation (black-dashed line). b) Transmittance intensity (green line) gained from the analytical model and its decomposition into electric (blue) and magnetic (red) dipole contributions. The parameters for the electric and magnetic dipole response are: $\lambda_{\text{mag}} = 1275$ nm, $\gamma_{\text{mag}} = 2\pi 6.8$ THz, and $\lambda_{\text{el}} = 1251$ nm, $\gamma_{\text{el}} = 2\pi 14.1$ THz. c) Numerically calculated transmittance for a Huygens' metasurface ($r_d = 242$ nm, $h = 220$ nm) embedded in a homogeneous medium with optimized refractive index ($n = 1.66$). The transmittance intensity (red solid line) and transmittance phase (blue solid line) for resonance overlap at $\lambda_{\text{el}, n=1.66} \approx \lambda_{\text{mag}, n=1.66} \approx 1340$ nm feature a transmission above $T_{\text{min}} \approx 0.995$ and full phase coverage of 2π .

record resonant transmission efficiencies of more than 55%. The slight deviations between the measured and simulated transmittance can be attributed to sample imperfections as well as to the finite numerical aperture of the microscope objective used in the experiments. We also model this case with our analytical model [see Figure 5b] which is in excellent agreement with the results shown in Figure 5a. Our analytical model also allows us to quantify the contributions of the electric and the magnetic resonance to the transmission spectrum and we find that a flat unity transmittance is not achieved here since the resonance widths of the electric and magnetic resonance are significantly different.

However, the spectral widths of the resonances and, therefore, the performance of the Huygens' metasurface can be improved by the appropriate choice of the dielectric environment since the refractive-index contrast between the nanodisk and the surrounding medium mainly determines the mode confinement of the two resonances. The spectral positions of the two resonances can be adjusted by geometrical tuning of the nanodisk dimensions. In this way, we can control both the resonance positions and the resonance widths of the Huygens' metasurface. As a result, the theoretical limit, i.e., near-unity transmission efficiencies, can be readily achieved for a Huygens' metasurface embedded in a dielectric medium with a refractive index of $n = 1.66$. We note that these optimized conditions can be realized using a variety of transparent high-index polymers.^[40] These results are shown in Figure 5c. For the condition of spectral overlap ($\lambda_{\text{el}} \approx \lambda_{\text{mag}}$) with a nanodisk radius of $r_d \approx 242$ nm we, then, observe a nearly flat spectrum (red line) with a resonant transmission value larger than 99% – naturally near-unity transmission is equivalent to near-zero absorption and reflection. As expected, also the 2π phase coverage (blue line) is preserved. Finally, to estimate the robustness of the 2π phase coverage against (experimental) variations of the disk radius and hence nonideal spectral overlap of the electric and magnetic resonances we calculate the transmittance phase and transmittance amplitude (color coded) of this Huygens' metasurface for a variation of the nanodisk radius ranging from 120 to 320 nm at a constant nanodisk height of $h = 220$ nm

(see Figure 6). The lattice constant is set as $a = 1.38 \times 2 \times r_d$. Remarkably, when evaluating the numerical results shown in Figure 6, we can identify a spectral range of about 400 nm, corresponding to a tolerance of about $r_d \approx 85$ nm in the nanodisk radius where the 2π phase coverage is preserved.

4. Wave-Front Engineering and Dispersion Control

In the following, we provide a glimpse of the technical potential that could be unlocked by all-dielectric optical Huygens' metasurfaces by presenting numerical and analytical model calculations for two different application areas:

First, all-dielectric Huygens' metasurfaces are ideally suited for efficient wave-front manipulation based on their capability to create a desired discrete phase gradient between 0 and 2π . Prominent application examples are beam deflection, beam shaping, and beam focusing as well as optical holography [Figure 7a]. For illustration of this concept, we choose the example of a linear phase gradient, as required for, e.g., a beam deflector, a Bessel-beam converter, or for a 2D-hologram. We calculate spectrally resolved relative phase delays for a systematic scaling of the nanodisks [Figure 7b] and detail the phase delays accessible at a wavelength of $\lambda \approx 1358$ nm [Figure 7c]. We then exemplarily use a five-element, equidistant phase discretization and identify the corresponding nanodisk radii required for full phase coverage. Remarkably, the transmission efficiency for this case is larger than $T = 96\%$ over the entire 2π phase range [see inset in Figure 7c].

The second example targets applications such as multiphoton microscopy and lithography, where the dispersion introduced by the focusing optics leads to a critical broadening of the pulse width of the exciting laser. Hence, prism, grating, or multiple-cycle chirped-mirror pulse compressors are required that are usually bulky and rely on precise (angular) alignment. We analytically show that an all-dielectric Huygens' metasurface can be utilized as a thin, compact, and highly efficient pulse-compression device [Figure 7d] since it provides a strong group-delay dispersion (GDD) of more than -2000 fs²

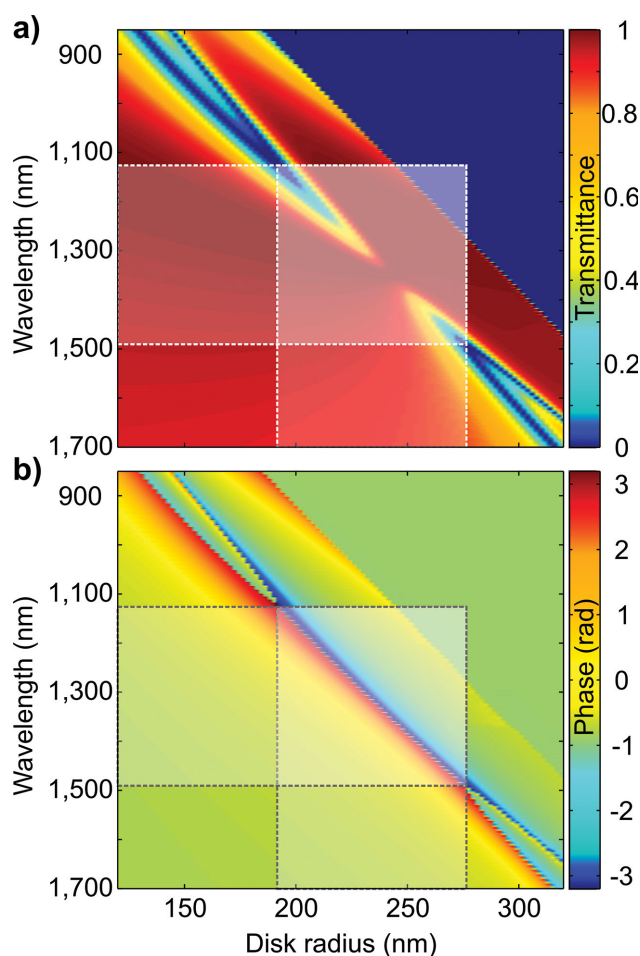


Figure 6. a) Numerically calculated transmittance intensity and b) transmittance phase (color coded) for a varying nanodisk radius r_d at a constant nanodisk height ($h = 220$ nm) for silicon-nanodisk metasurfaces embedded in a homogeneous medium with $n = 1.66$. The white-shaded area indicates the spectral region and nanodisk radius range where full 2π phase coverage can be achieved. The ideal spectral-overlap case featuring transmission above $T_{\min} \approx 0.995$ and full phase coverage of 2π is obtained for a nanodisk radius $r_d = 242$ nm at $\lambda_{\text{el}, n=1.66} \approx \lambda_{\text{mag}, n=1.66} \approx 1340$ nm [see also Figure 5c)].

[Figure 7e] in combination with unity transmission. For our calculations, we concentrate on the practically important case of compressing a chirped 120-fs laser pulse at $\lambda = 800$ nm wavelength. Figure 7f shows that a 120 fs chirped pulse – the chirp corresponds to propagation through 20 cm of glass, e.g., in a typical two-photon microscope – is almost completely recompressed to the Fourier-limited initial pulse after transmission through six layers of our Huygens' metasurface. This shows that Huygens' metasurfaces can also provide remarkable dispersion-control that can be integrated in a linear beam path as an ultrathin transmitting element.

5. Conclusion

In summary, we have experimentally demonstrated, for the first time to our knowledge, an all-dielectric Huygens' metasurface operating at near-IR frequencies. In contrast to earlier

works on mode properties and mode tuning of silicon nanodisks, our direct measurements of the transmittance-phase of Huygens' metasurfaces consisting of subwavelength arrays of silicon-nanodisk metaatoms reveal that our new concept provides full phase coverage from 0 to 2π while, at the same time, showing record resonant transmission efficiencies of more than 55%. We further demonstrate that transmission efficiencies very close to 100% can be achieved for a realistic choice of the embedding dielectric medium and analytically identify that the unique properties of our Huygens' metasurface have their foundations in the resonant overlap of electric and magnetic dipole resonances of the silicon-nanodisk resonators. The observed effect is polarization independent, polarization preserving, robust, and the operation wavelength can be scaled by the geometrical parameters of the nanodisk metasurface. Our results establish all-dielectric Huygens' metasurfaces as ideal candidates for near-unity-efficiency light-wave manipulation providing full phase coverage with negligible reflection and absorption losses. Therefore, they offer a practical route for the implementation of a multitude of transmitting optical devices, including flat optics, optical holography, and dispersion control applications.

Importantly, our proposed Huygens' metasurfaces are fully compatible with standard industrial silicon technology and, due to the simple disk-shape of the metaatom, also suitable for large-area fabrication techniques such as interference lithography, nanoimprint lithography, and conventional optical lithography.

6. Experimental Section

Fabrication: For fabrication we have performed electron-beam lithography on silicon-on-insulator wafers (SOITEC, 220 nm top silicon thickness, 2 μm buried oxide thickness, backside polished) using the negative-tone resist NEB-31A and hexamethyldisilazane (HMDS) as adhesion promoter. Development was performed by inserting the sample into MF-321 developer. The resulting resist pattern was used as an etch mask for a directive reactive-ion etching process. Residual resist was removed using oxygen plasma. The sample footprints are 2 mm \times 2 mm to allow for transmittance-phase measurements.

Transmittance Measurements: The transmittance-intensity, i.e., the spectrally resolved transmitted power, was collected by a white-light spectroscopy setup connected to an optical spectrum analyzer. A tungsten-halogen lamp was used as a broadband light source. The range of incident angles has been reduced to $\pm 6^\circ$ by an aperture. The experimental transmittance-intensity T was referenced to the transmittance-intensity of the unstructured etched wafer T_{Ref} . For transmittance-phase measurements we used a home-built interferometry setup.^[37,38] In this setup a white-light beam from a supercontinuum source is divided into two parallel beams (sample and reference beams) by a polarizing beam displacer. The wafer with the silicon-nanodisk fields was inserted into the beam path in such a way that the sample beam was passing through the respective field to be measured and the reference beam was passing through an unstructured area of the wafer next to the field. After transmission through the wafer the two beams were recombined using a second polarizing beam displacer and sent to a spectrometer.

Analytical Coupled-Dipole Model: Each silicon-nanodisk metaatoms is modeled as electric and magnetic dipoles oriented in x and y direction with specific polarizabilities α^e and α^m that are arranged in an infinite subwavelength 2D-square lattice [see Figure 1a]. For x -polarized illumination with a plane wave propagating in $-z$ direction $\mathbf{E}(z, t) = \mathbf{E}_0$

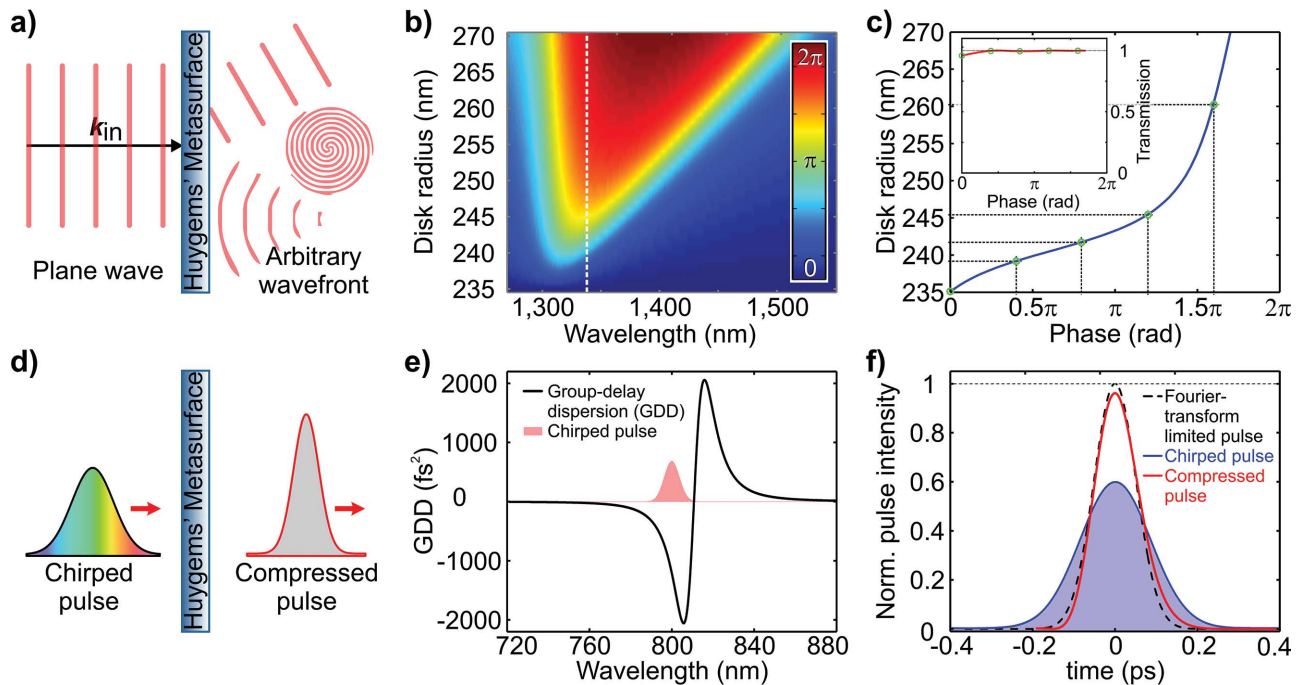


Figure 7. a) Schematic of a Huygens' metasurface for unity-efficiency wave-front manipulation. b) Calculated phase-delay spectrum (color coded) of silicon-nanodisk Huygens' metasurfaces with radii $r_d = 235\text{--}267\text{ nm}$ and a constant aspect ratio $r_d/h = 1.21$ ($n = 1.66$) referenced to the phase delay for $r_d = 235\text{ nm}$. c) Phase-delay values accessible for $\lambda = 1338\text{ nm}$ [white-dashed line in b)]. The selections of nanodisk radii providing a linear phase gradient with a five-element discretization are plotted over the respective phase-delay values. The transmission (red line) at these points (green circles) is shown in the inset. d) Scheme showing the recompression of a chirped pulse after passing a Huygens' metasurface. e) GDD for an ideal Huygens' metasurface resonant at $\lambda_{el} = \lambda_{mag} \approx 811\text{ nm}$ (black solid line) and the spectrum of a chirped laser pulse (red-shaded area). The model parameters $\lambda_{el} = \lambda_{mag} \approx 811\text{ nm}$ and $\gamma_e = \gamma_m = 4\text{ THz}$ are extracted from Figure 5 c) to provide a realistic estimate. f) Temporal profile of a 120-fs Fourier-limited pulse, of the chirped pulse, and of the recompressed pulse after propagation through six layers of the Huygens' metasurface.

$\exp(-ik_d z - i\omega t)$, where k_d is the wavevector of light in the medium, the mutual interactions between the individual dipoles of the metasurface result in an electric and magnetic dipole moment \mathbf{p} and \mathbf{m} given by^[34]

$$\mathbf{p} = \alpha^e \left[\mathbf{E}_0 + \frac{k_0^2}{\epsilon_0} \hat{\mathbf{G}}^0 \cdot \mathbf{p} \right] \quad (3)$$

$$\mathbf{m} = \alpha^m \left[\mathbf{H}_0 + k_0^2 \epsilon_d \hat{\mathbf{G}}^0 \cdot \mathbf{m} \right] \quad (4)$$

Here, $\hat{\mathbf{G}}^0 = \sum_{j=1}^{\infty} \mathbf{G}_{0j}$ is the sum of the Green's functions of the single electric/magnetic dipoles at a position j in the square lattice and takes into account effects arising from the periodic arrangement of the dipoles such as the mutual interaction of the single electric and magnetic dipoles in the lattice and the appearance of diffraction. In the metamaterial limit, however, i.e., for lattice constants smaller than the wavelength of the incident light, the influence of radiative interactions between the dipoles can be neglected and the scattering is ultimately determined by the scattering properties of the individual particles^[34] with the corresponding effective electric/magnetic polarizabilities $\alpha_{eff}^{e,m}$.

Starting from the electric and magnetic dipole moments given above, one can calculate the total electric far-field response outside of the metasurface which consist of the superposition of the incident field and the scattered field from the electric and the magnetic response of the nanodisk metasurface. For an incident polarization of the electric field vector along x or y direction, this finally results in a transmittance coefficient of the metasurface given by

$$t = 1 + \frac{ik_d}{2A} (\alpha_{eff}^e + \alpha_{eff}^m) \quad (5)$$

A is the area of a unit cell, $k_d = n_d \cdot \omega / c_0$ is the wavevector of light in a medium with the refractive index n_d , and $\alpha_{eff}^e = 1 / (\epsilon_0 \epsilon_d / \alpha^e - k_0^2 \hat{\mathbf{G}}^0)$ and $\alpha_{eff}^m = 1 / (1 / \alpha^m - k_d^2 \hat{\mathbf{G}}^0)$ are the effective (electric and magnetic) polarizabilities of the metasurface.

To connect this expression with experimental transmittance spectra, we describe the dispersion of the effective electric and magnetic polarizabilities (α_{eff}^e and α_{eff}^m) by Lorentzian line shapes given by

$$\alpha_{eff}^e = \frac{\alpha_0^e}{\omega_e^2 - \omega^2 - 2i\gamma_e \omega} \quad (6)$$

$$\alpha_{eff}^m = \frac{\alpha_0^m}{\omega_m^2 - \omega^2 - 2i\gamma_m \omega} \quad (7)$$

In a final step, the amplitudes of the effective polarizability amplitudes $\alpha_0^{e,m}$ have to be determined. For spectrally well-separated resonances both the electric and the magnetic resonances are pronounced resonance dips at $\omega = \omega_e$ and $\omega = \omega_m$, ideally reaching zero transmittance $T = 0$. For this case, the transmittance can be written as

$$T = |t(\omega_{e,m})|^2 = \left| 1 + \frac{ik_d}{2A} \alpha_{eff}^{e,m}(\omega_{e,m}) \right|^2 = 0 \quad (8)$$

and we can determine the polarizability amplitudes $\alpha_0^{e,m} = \frac{4Ac_0}{n_d} \gamma_{e,m}$.

Finally we can calculate an analytical expression for the (field-) transmittance coefficient of a metasurface:

$$t = 1 + \frac{2i \cdot \gamma_e \omega}{\omega_e^2 - \omega^2 - 2i\gamma_e \omega} + \frac{2i \cdot \gamma_m \omega}{\omega_m^2 - \omega^2 - 2i\gamma_m \omega} \quad (9)$$

The (field-) reflection coefficient is obtained accordingly

$$r = \frac{2i \cdot \gamma_e \omega}{\omega_e^2 - \omega^2 - 2i\gamma_e \omega} - \frac{2i \cdot \gamma_m \omega}{\omega_m^2 - \omega^2 - 2i\gamma_m \omega} \quad (10)$$

Numerical Calculations: Numerical calculations are performed using the finite-integral frequency-domain solver provided by the commercially available software package CST Microwave Studio. The silicon refractive index is taken as 3.5, that of the buried oxide layer as 1.45, and the refractive indices of the embedding media are $n = 1.4$ and $n = 1.66$, respectively. All materials are assumed to be loss-less and dispersion-less. We use unit cell boundary conditions and normal incidence plane-wave excitation.

Supporting Information

Supporting Information is available from the Wiley Online Library or from the author.

Acknowledgements

We acknowledge useful discussions with W. Liu, A. E. Miroshnichenko, M. Wegener, J. Fischer, D. Powell, V. Stoev, and A. Evlyukhin. This work was performed, in part, at the Center for Integrated Nanotechnologies, an Office of Science User Facility operated for the U.S. Department of Energy (DOE) Office of Science. Sandia National Laboratories is a multiprogram laboratory managed and operated by Sandia Corporation, a wholly owned subsidiary of Lockheed Martin Corporation, for the U.S. Department of Energy's National Nuclear Security Administration under Contract No. DE-AC04-94AL85000. The authors also acknowledge support from the Australian Research Council through Discovery Project and DECRA Fellowship grants as well as support from the Group of Eight: Australia – Germany Joint Research Cooperation Scheme, the German Federal Ministry of Education and Research (PhoNa), and the Thuringian Ministry of Education, Science and Culture (MeMa).

Received: December 7, 2014

Revised: January 8, 2015

Published online: February 1, 2015

- [1] C. Huygens, *Traité de la Lumière*, Pieter van der Aa, Leyden 1690.
- [2] A. E. H. Love, *Philos. Trans. R. Soc. London A* **1901**, 197, 1.
- [3] A. D. Yaghjian, in the 3rd European Conference on Antennas and Propagation, EuCAP2009, Berlin, Germany **2009**.
- [4] J. M. Geffrin, B. Garcia-Camara, R. Gomez-Medina, P. Albella, L. S. Froufe-Perez, C. Eyraud, A. Litman, R. Vaillon, F. Gonzalez, M. Nieto-Vesperinas, J. J. Saenz, F. Moreno, *Nat. Commun.* **2012**, 3, 1171.
- [5] C. Pfeiffer, A. Grbic, *Phys. Rev. Lett.* **2013**, 110, 197401.
- [6] F. Monticone, N. M. Estakhri, A. Alu, *Phys. Rev. Lett.* **2013**, 110, 203903.
- [7] C. Pfeiffer, N. K. Emani, A. M. Shaltout, A. Boltasseva, V. M. Shalae, A. Grbic, *Nano Lett.* **2014**, 14, 2491.
- [8] C. Enkrich, M. Wegener, S. Linden, S. Burger, L. Zschiedrich, F. Schmidt, J. F. Zhou, T. Koschny, C. M. Soukoulis, *Phys. Rev. Lett.* **2005**, 95, 203901.
- [9] S. Muehlig, C. Menzel, C. Rockstuhl, F. Lederer, *Metamaterials* **2011**, 5, 64.
- [10] Aldo Petosa, A. Ittipiboon, *IEEE Antennas Propag.* **2010**, 52, 91.
- [11] C. F. Bohren, D. R. Huffman, *Absorption and Scattering of Light by Small Particles*, John Wiley & Sons Inc., New York, USA **1983**.
- [12] Q. Zhao, J. Zhou, F. Zhang, D. Lippens, *Mater. Today* **2009**, 12, 60.
- [13] A. B. Evlyukhin, S. M. Novikov, U. Zywietz, R. L. Eriksen, C. Reinhardt, S. I. Bozhevolnyi, B. N. Chichkov, *Nano Lett.* **2012**, 12, 3749.
- [14] A. I. Kuznetsov, A. E. Miroshnichenko, Y. H. Fu, J. Zhang, B. Luk'yanchuk, *Sci. Rep.* **2012**, 2, 492.
- [15] Y.-H. Fu, A. I. Kuznetsov, A. E. Miroshnichenko, Y. F. Yu, B. Luk'yanchuk, *Nat. Commun.* **2013**, 4, 1527.
- [16] S. Person, M. Jain, Z. Lapin, J. J. Saenz, G. Wicks, L. Novotny, *Nano Lett.* **2013**, 13, 1806.
- [17] J. C. Ginn, I. Brener, D. W. Peters, J. R. Wendt, J. O. Stevens, P. F. Hines, L. I. Babilio, L. K. Warne, J. F. Ihlefeld, P. G. Clem, M. B. Sinclair, *Phys. Rev. Lett.* **2012**, 108, 097402.
- [18] P. Spinelli, M. A. Verschuuren, A. Polman, *Nat. Commun.* **2012**, 3, 692.
- [19] I. Staude, A. E. Miroshnichenko, M. Decker, N. T. Fofang, S. Liu, E. Gonzales, J. Dominguez, T. S. Luk, D. N. Neshev, I. Brener, Yu. S. Kivshar, *ACS Nano* **2013**, 7, 7824.
- [20] B. Slovick, Z. G. Yu, M. Berding, S. Krishnamurthy, *Phys. Rev. B* **2013**, 88, 165116.
- [21] C. Wu, N. Arju, G. Kelp, J. A. Fan, J. Dominguez, E. Gonzales, E. Tutuc, I. Brener, G. Shvets, *Nat. Commun.* **2014**, 5, 3892.
- [22] N. Yu, P. Genevet, M. A. Kats, F. Aieta, J.-P. Tetienne, F. Capasso, Z. Gaburro, *Science* **2011**, 334, 333.
- [23] X. Ni, N. K. Emani, A. V. Kildishev, A. Boltasseva, V. M. Shalae, *Science* **2012**, 335, 427.
- [24] L. Huang, X. Chen, H. Muehlenbernd, G. Li, B. Bai, Q. Tan, G. Jin, T. Zentgraf, S. Zhang, *Nano Lett.* **2012**, 12, 5750.
- [25] M. Kang, T. Feng, H. T. Wang, J. Li, *Opt. Express* **2012**, 20, 15882.
- [26] F. Aieta, P. Genevet, M. A. Kats, N. Yu, R. Blanchard, Z. Gaburro, F. Capasso, *Nano Lett.* **2012**, 12, 4932.
- [27] X. Chen, L. Huang, H. Muehlenbernd, G. Li, B. Bai, Q. Tan, G. Jin, C.-W. Qiu, S. Zhang, T. Zentgraf, *Nat. Commun.* **2012**, 3, 1198.
- [28] L. Huang, X. Chen, H. Muehlenbernd, H. Zhang, S. Chen, B. Bai, Q. Tan, G. Jin, K.-W. Cheah, C.-W. Qiu, J. Li, T. Zentgraf, S. Zhang, *Nat. Commun.* **2013**, 4, 2808.
- [29] Y. Yang, W. Wang, P. Moitra, I. I. Kravchenko, D. P. Briggs, J. Valentine, *Nano Lett.* **2014**, 14, 1394.
- [30] S. Larouche, Y.-J. Tsai, T. Tyler, N. M. Jokerst, D. R. Smith, *Nat. Mater.* **2012**, 11, 450.
- [31] L. Zou, W. Withayachumnankul, C. M. Shah, A. Mitchell, M. Bhaskaran, S. Sriram, C. Fumeaux, *Opt. Express* **2013**, 21, 1344.
- [32] N. Yu, F. Capasso, *Nat. Mater.* **2014**, 13, 139.
- [33] Y. B. Li, X. Wang, B. G. Cai, Q. Cheng, T. J. Cui, *Sci. Rep.* **2014**, 4, 6921.
- [34] A. B. Evlyukhin, C. Reinhardt, A. Seidel, B. S. Luk'yanchuk, B. N. Chichkov, *Phys. Rev. B* **2010**, 82, 045404.
- [35] A. S. Schwanecke, V. A. Fedotov, V. V. Khardikov, S. L. Prosvirnin, Y. Chen, N. I. Zheludev, *J. Opt. A: Pure Appl. Opt.* **2007**, 9, L1.
- [36] S. Liu, M. B. Sinclair, T. S. Mahony, Y. C. Jun, S. Campione, J. Ginn, D. A. Bender, J. R. Wendt, J. F. Ihlefeld, P. G. Clem, J. B. Wright, I. Brener, *Optica* **2014**, 4, 247.
- [37] E. Pshenay-Severin, F. Setzpfandt, C. Helgert, U. Huebner, C. Menzel, A. Chipouline, C. Rockstuhl, A. Tuennermann, F. Lederer, T. Pertsch, *J. Opt. Soc. Am. B* **2010**, 27, 660.
- [38] E. Pshenay-Severin, M. Falkner, C. Helgert, T. Pertsch, *Appl. Phys. Lett.* **2014**, 104, 221906.
- [39] E. Hallynck, P. Bienstman, *IEEE Photonics J.* **2012**, 4, 443.
- [40] J.-G. Liu, M. Ueda, *J. Mater. Chem.* **2009**, 19, 8907.